Diagonalizing the Softmax: Hadamard Initialization for Tractable Cross-Entropy Dynamics

Connall Garrod [1] **Jonathan P. Keating** [1] **Christos Thrampoulidis** [2]

Abstract

In this work, we study cross-entropy (CE) dynamics using a two-layer linear network with orthogonal inputs, the simplest non-convex setting where the CE implicit bias remains unresolved. This coincides with the unconstrained features model used to study neural collapse (NC). Our analysis is based on a key observation: Hadamard initialization diagonalizes the softmax operator. This allows us to extend the spectral initialization framework that Saxe et al. (2013; 2019) developed for squared loss. We prove convergence to NC under spectral CE training and give the first finite-time analysis in this setting via an explicit Lyapunov function that decreases monotonically to NC. We further identify CE-specific phenomena absent under squared loss, and show empirically that spectral dynamics qualitatively model small random initialization.

1. Introduction

The training dynamics of linear networks under mean squared error (MSE) loss have been studied extensively. Among the most far-reaching works is the spectral-dynamics framework initiated by Saxe et al. (2013; 2019). In these analyses, gradient flow is reduced to a tractable evolution of singular values, yielding closed-form training trajectories. A central strength of these works is that they model the full optimization trajectory, rather than only asymptotic characterizations.

No comparable trajectory-level theory is known for classification with cross-entropy (CE) loss. The obstruction is the softmax, which nonlinearly couples singular values, preventing the spectral reductions that make MSE dynamics tractable. Even simple non-convex CE models remain out of reach. *Can the techniques developed for linear MSE networks be extended to CE with softmax activation?*

This gap is important because we still lack a trajectory-level understanding of several phenomena specific to classification. The most striking example is the geometric phenomenon of neural collapse (NC) (Papyan et al., 2020): in deep networks class-mean embeddings and final layer weights converge to a simplex equiangular tight frame (ETF). This geometry appears across a range of architectures and datasets, despite the absence of any explicit mechanism enforcing it. *What mechanism in gradient-based optimization selects this precise geometric configuration from among the many solutions that achieve vanishing training loss?*

This question lies within the framework of *implicit bias*, but existing theory remains largely confined to asymptotic analyses. Before reaching its limit, a trajectory may exhibit rich transient behavior, and convergence to the asymptotic regime may be so slow that limiting descriptions miss the dynamics that occur at practical timescales. A complete account of implicit bias in this setting therefore requires understanding the entire trajectory of optimization.

We give the first *trajectory-level* analysis of multiclass CE training dynamics for the CE unconstrained feature model (UFM), a model popular in the NC literature that also represents the simplest non-convex model for which the implicit bias remained unknown: a two-layer linear network with orthogonal inputs.

Softmax diagonalization. We show that Hadamard initialization diagonalizes the softmax nonlinearity. This enables us to extend the framework of Saxe et al. (2013; 2019) from MSE to CE, reducing gradient flow to a vector ODE over the singular values of the logit matrix that is sufficiently structured for a study of gradient flow trajectories.

Non-monotonicity. Unlike MSE, CE can exhibit non-monotonic behavior that depends on the number of classes K and that is invisible to asymptotic analyses.

Guaranteed convergence to NC. Despite the non-monotonicity of natural metrics and the non-convex land-

[1]Mathematical Institute, University of Oxford [2]Department of Electrical and Computer Engineering, University of British Columbia. Correspondence to: Connall Garrod <connall.garrod@maths.ox.ac.uk>, Christos Thrampoulidis <cthrampo@ece.ubc.ca>.

Workshop on Weight-Space Symmetries, held in conjunction with the 43rd International Conference on Machine Learning, Seoul, South Korea. 2026. Copyright 2026 by the author(s).

scape, we prove that gradient flow *always* converges to NC under Hadamard initialization. Unlike asymptotic arguments, we provide an explicit Lyapunov function that decreases monotonically along the full trajectory.

The Hadamard trajectories we analyze are genuine gradient-flow paths, so the phenomena above are compatible with CE training. Empirically, we show these trajectories also qualitatively model small random initialization.

Related work. Many works study the emergence of NC through the UFM (Mixon et al., 2020). For CE, existing analyses rely on explicit L_2 regularization (Zhu et al., 2021; Garrod & Keating, 2024a), or establish convergence only to a KKT point (Ji et al., 2022). Previous implicit bias results have shown that logistic regression converges to the max-margin solution (Soudry et al., 2018). Subsequent work has extended this to homogeneous networks (Lyu & Li, 2019; Ji & Telgarsky, 2019; 2020) through KKT characterizations. For spectral dynamics, Saxe et al. (2013) showed that deep linear networks trained with MSE loss can admit tractable explicit dynamics over singular modes. This framework has since been extended to studies of emergence (Saxe et al., 2019), initialization (Braun et al., 2022; Kunin et al., 2024), optimization (Gidel et al., 2019), training (Domin'e et al., 2024), and linear attention (Mainali & Teixeira, 2025).

2. Background

Consider K-class classification with n samples per class. Let $h_{ic} \in \mathbb{R}^d$ denote the embedding, parameterized by a deep network, of sample $i \in [n]$ from class $c \in [K]$. Stack these by class to form the embedding matrix $H \in \mathbb{R}^{d \times Kn}$, and let $W \in \mathbb{R}^{K \times d}$ denote the last layer classifier head.

Neural collapse (NC) (Papyan et al., 2020) is the empirically observed phenomenon wherein $H^\top H \propto S \otimes 1_n 1_n^\top$ and $WW^\top \propto S$, where $\otimes$ is the Kronecker product and $S = I_K - \frac{1}{K} 1_K 1_K^\top \in \mathbb{R}^{K \times K}$ is the simplex ETF matrix.

Unconstrained Features Model. The UFM approximates an expressive deep network by treating the embedding h_{ic} of the data as freely optimized vectors. Under CE loss, the UFM minimizes over $W \in \mathbb{R}^{K \times d}$, $H \in \mathbb{R}^{d \times Kn}$:

$$\mathcal{L} = \sum_{c \in [K], i \in [n]} \log\left(1 + \sum\nolimits_{c' \neq c} e^{(Wh_{ic})_{c'} - (Wh_{ic})_c}\right). \quad (1)$$

This can be viewed as a two-layer linear network with weights W and H, and input data the standard basis vectors in $\mathbb{R}^{Kn}$. See App. A of Garrod & Keating (2024b) for discussion on the UFM as a modeling tool.

Let $Y = I_K \otimes 1_n^\top \in \mathbb{R}^{K \times nK}$ denote the one-hot label matrix. Define $P(Z)$ to be the *softmax* operation applied to the logit matrix $Z = WH$: i.e., $\left[P(Z)\right]_{ij} = \exp(Z_{ij}) \big/ \sum_{k=1}^K \exp(Z_{kj})$. Under gradient flow on the CE loss in Eq. (1), the parameters evolve according to

$$\frac{dW}{dt} = (Y - P(Z))H^T, \quad \frac{dH}{dt} = W^T(Y - P(Z)). \quad (2)$$

Whilst Ji et al. (2022) showed that this gradient flow converges directionally to a KKT point of a max-margin problem, and characterized the KKT points, gradient flow can, in general, converge to KKT points that are not even local minima of the non-convex max-margin problem (Vardi et al., 2022). This is because the true loss surface features no finite minima, and arguments about avoiding saddles (Lee et al., 2019) do *not* apply. Thus, the question is open: *Does gradient flow* (2) *converge to NC solutions?*

Exact dynamics with MSE loss. Replacing CE with MSE makes the UFM analytically tractable, thanks to Saxe et al. (2013; 2019). Under MSE loss, gradient flow is instead:

$$\frac{dW}{dt} = (Y - WH)H^T, \qquad \frac{dH}{dt} = W^T(Y - WH). \quad (3)$$

Let the SVD of Y be $Y = U\Sigma V^T$, with singular values s_c for $c \in [K]$. Consider spectral initialization: $W = UD_W R^T, H = RD_H V^T$, for orthogonal $R \in \mathbb{R}^{d \times d}$, with D_W and D_H having their only non-zero diagonal entries being $\alpha_1, ..., \alpha_K$ and $\beta_1, ..., \beta_K$. Then, at initialization, the label matrix Y and the logit matrix WH are mutually diagonalizable. When used in Eq. (3), this implies that $\frac{dW}{dt}, \frac{dH}{dt}$ have the same singular vectors as W, H. Thus, only the singular values of W and H evolve, and can be shown to monotonically approach s_i along sigmoidal trajectories. Saxe et al. (2013) further show empirically that small random initialization has the same characteristic behavior as these analytic paths. *Can this framework extend to CE loss?*

3. Hadamard initialization

The obstacle in extending spectral dynamics from MSE to CE is the softmax nonlinearity: for CE we must simultaneously diagonalize Y, WH and $P(WH)$, which is difficult since nonlinearities rarely preserves spectral structure. This obstacle can be overcome by using Hadamard initialization.

Definition 3.1. The **Sylvester Hadamard matrices** $\{\Phi_{2^m} : m \in \mathbb{N}\}$ are defined recursively by

$$\Phi_1 = 1, \quad \Phi_{2^m} = \begin{bmatrix} \Phi_{2^{m-1}} & \Phi_{2^{m-1}} \\ \Phi_{2^{m-1}} & -\Phi_{2^{m-1}} \end{bmatrix} \in \mathbb{R}^{2^m \times 2^m}.$$

Each Φ_{2^m} is a ± 1-valued matrix, whose first row/column consist entirely of ones. Moreover, they are symmetric $\Phi_{2^m}^T = \Phi_{2^m}$ and orthogonal $\Phi_{2^m}^T \Phi_{2^m} = 2^m I_{2^m}$. Sylvester Hadamard matrices form a subclass of the more general Hadamard matrices; the study of which is left to future work.

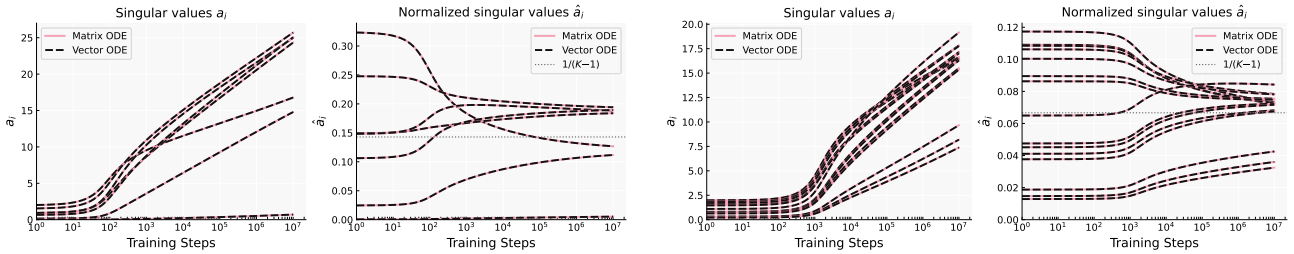

(a) $K = 8$ (b) $K = 16$

Figure 1. Numerical illustration of the Hadamard reduction for $K = 8, 16$. The trajectories of the full matrix dynamics (Eq. (2)) and the reduced vector ODE (Eq. (4)) are indistinguishable, verifying Thms. 3.2 and 3.3.

We first illustrate our technique for $n = 1$ (one data point per class), then extend to general n. In this case, the label matrix reduces to $Y = I_K$. We show that setting $U = \frac{1}{\sqrt{K}}\Phi$ achieves mutual diagonalizability despite the softmax.

Theorem 3.2. *For $K = 2^m, m \in \mathbb{N}$, let $U = \frac{1}{\sqrt{K}}\Phi$, where Φ is the $K \times K$ Sylvester Hadamard matrix. Denote the columns of U by u_i, $i \in [K]$. Then, for any $Z = \sum_i a_i u_i u_i^T$, its softmax satisfies*

$$P(Z) = \sum\nolimits_i \nu_i u_i u_i^T, \quad \textit{where} \;\; \nu_i = \frac{\sum_j \Phi_{ij} e^{\frac{1}{K}(\Phi a)_j}}{\sum_j e^{\frac{1}{K}(\Phi a)_j}}.$$

We refer to this initialization as *Hadamard initialization*. This shows that spectral structure is preserved: a matrix diagonalizable by a Sylvester–Hadamard matrix remains so after applying softmax. See App. B.1 for a detailed proof.

3.1. Tractable cross-entropy dynamics

Using Theorem 3.2, we can adapt the arguments of Saxe et al. (2013), detailed in Sec. 2. This property is specific to our construction: a generic orthogonal U does not yield mutual diagonalizability. The result is given for general n below. The proof is in App. B.2, with validation in Fig. 1.

Theorem 3.3. *For $K = 2^m, m \in \mathbb{N}$, let $U = \frac{1}{\sqrt{K}}\Phi$. For the UFM in Eq. (1), with classes of size n, initialize the parameters as $W = UD_W R^T$, and $H = RD_H V^T$, where $R \in \mathbb{R}^{d\times d}$ is orthogonal, $V = U \otimes Q$ where Q is a right singular matrix of 1_n^T, and the only nonzero singular values of D_W and D_H are $\alpha_0, \dots, \alpha_{K-1}$ and $\beta_0, \dots, \beta_{K-1}$. Then under balancedness, and absorbing constants into the time and singular value variables, the gradient flow equations reduce to*

$$\frac{da_i}{dt} = \frac{1}{D} b_i a_i \quad i \in [K-1], \quad \frac{da_0}{dt} = 0, \tag{4}$$

$$b_i = \sum_{j=1}^{K-1} \Psi_{ij} e^{-(\Psi a)_j} \;\; \textit{and} \;\; D = 1 + \sum_{j=1}^{K-1} e^{-(\Psi a)_j} \tag{5}$$

where $a_i = \alpha_i \beta_i$ are the logit singular values, and $\Psi = 1_{K-1}1_{K-1}^T - \Phi[2:K, 2:K] \in \mathbb{R}^{K-1\times K-1}$.

Since the first singular value is constant, we drop it from notation and consider $a \in \mathbb{R}^{K-1}$. We now describe essential features of these dynamics:

Coupled dynamics. Unlike the MSE case, the terms b_i/D depend on the complete set of singular values $a_1, \dots, a_{K-1}$. The equations therefore do not decouple, and each singular value influences the trajectory of the others. Because of this, there are not enough conserved quantities to guarantee closed-form dynamics. Nevertheless, we show below that they are sufficiently tractable.

Positive singular values. The singular values $a_i(t)$ are monotonically increasing in time. Therefore, if $a_i(0) > 0$, then $a_i(t) > 0$ for all $t \geq 0$. Moreover, if $a_i(0) = 0$, then it remains zero throughout training. We henceforth assume all singular values are initialized to positive values.

Normalized singular values. From Eq. (4), it is straightforward to show that the norm of the logit singular values (e.g., the L_1-norm $\|a\|_1 = \sum_i a_i$) diverges to infinity. This divergence implies that there are no finite minima of the UFM objective on the optimization surface. We therefore study the dynamics of the *normalized logit singular values* $\hat{a}_i = a_i/\|a\|_1$, which evolve as:

$$\frac{d}{dt}(\hat{a}_i) = \frac{\hat{a}_i}{D}\left[b_i - \bar{b}\right], \quad \text{where } \bar{b} = \sum\nolimits_{j\in[K-1]} \hat{a}_j b_j. \tag{6}$$

Note that the normalized logit singular value vector $\hat{a}$ lies on the $K-1$ dimensional simplex, since with positive initialization all entries remain positive throughout the dynamics.

4. Cross-entropy dynamics and implicit bias

Any direction $\hat{a}$ satisfying $(\Psi\hat{a})_i > 0$ for all $i \in [K-1]$ will have positive margins and so can attain arbitrarily small loss by taking $\|a\|_1 \to \infty$. The key question is therefore which of these zero-loss directions gradient flow selects. We begin by inspecting the *stable directions*, i.e., those satisfying $\frac{d\hat{a}}{dt} = 0$. If a stable direction satisfies $\hat{a}_i > 0$ for all i, then the corresponding logit matrix is full-rank. It is simple to show the unique full-rank stable direction is $\hat{a} = \frac{1}{K-1}1_{K-1}$. This in fact corresponds to NC, since equal logit singular values implies under

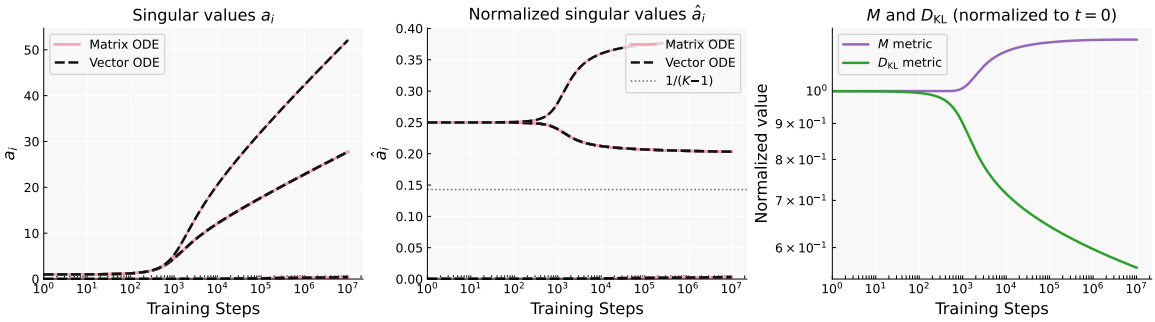

Figure 2. Training with $K = 8$ and $a(0) = [1, 1, 1, 1, 0.001, 0.001, 0.001]$. **Left/Middle:** Evolution of raw/normalized singular values. **Right:** Evolution of the metric M in Eq. (7) and the KL Lyapunov function of Thm. 4.1, both normalized by their initial values.

balancedness that the singular values of W, H are also equal. This then yields $W \propto \Phi\,\mathrm{diag}(0, 1, \ldots, 1)R^T$ and $H \propto R\,\mathrm{diag}(0, 1, \ldots, 1)\Phi^T$, which implies NC.

Convergence to NC via a Lyapunov function. Does gradient flow exhibit an implicit preference for the full-rank NC solution $\hat{a} = \frac{1}{K-1}1_{K-1}$ among all other stable points? We show that this is indeed the case. Moreover, we establish a stronger result than asymptotic convergence: we identify a Lyapunov function, measuring distance to NC, that decreases monotonically along the gradient-flow trajectory. The proof is in App. B.3.

Theorem 4.1. *Let $K = 2^m, m \in \mathbb{N}$. Let $a(t) \in \mathbb{R}^{K-1}$ be initialized with $a_i(0) > 0$ for all i, that evolves under the time evolution of Eq. (4). Then the metric $D_{\mathrm{KL}}(\frac{1}{K-1}1_{K-1} \,\|\, \hat{a})$, where D_{KL} is the Kullback-Leibler divergence, serves as a Lyapunov function of the flow. Consequently, the metric is decreasing throughout training and we must have $\hat{a} \to 1/(K-1) \cdot 1_{K-1}$ as $t \to \infty$.*

This result is notable in two respects. First, regarding *implicit bias*, existing results typically establish only asymptotic convergence rather than monotonic behavior throughout the full loss surface via a Lyapunov function. Even when restricted to asymptotic convergence, the only prior result applicable to the CE UFM (Ji & Telgarsky, 2019) is limited to binary classification ($K = 2$). However, the binary case is trivial in our framework: the unique stable direction (of rank $K - 1 = 1$) is NC itself. In contrast, for $K \geq 4$, multiple stable directions exist, making the implicit bias question nontrivial. Second, regarding *neural collapse*, all previous claims about convergence to NC either used explicit finite regularization (Zhu et al., 2021), analyzed the regularization path (Thrampoulidis et al., 2022), or characterized the KKT points of the corresponding non-convex max-margin problem (Ji et al., 2022). Theorem 4.1 is the first result proving that NC occurs purely as a result of gradient flow implicit bias under CE loss.

Non-monotonic behaviors. The monotonic convergence via a Lyapunov function is a special property. We now show that the L2-distance metric, which is common in empirical work on NC, does not exhibit monotonic behavior.

$$M = \frac{1}{2}\sum\nolimits_{i\in[K-1]}\left(\hat{a}_i - \frac{1}{K-1}\right)^2. \tag{7}$$

For $K = 2, 4$, this metric decreases monotonically; however, monotonicity breaks down for $K \geq 8$.

Theorem 4.2. *For $K = 2^m, m \in \mathbb{N}$, let $a(t) \in \mathbb{R}^{K-1}$ be a variable initialized with $a(0) > 0$, that evolves as in Eq. (4). If $K = 2$ or $K = 4$, then the metric M in Eq. (7) monotonically converges to 0. If $K \geq 8$, then there exist initializations $a(0)$ such that the metric M is not monotonic.*

The proof is in App. B.4. This result reveals a fundamental qualitative difference from MSE (Saxe et al., 2013; 2019): here, coupled singular values can induce non-monotonic behavior in natural distance metrics. Fig. 2 illustrates the severity of this phenomenon, showing the evolution of $\hat{a}_i$ and M for an initialization leading to non-monotonic behavior: M increases monotonically over the displayed trajectory, even if it must eventually go to zero.

The role of non-uniform stable points ($K \geq 8$). This behavior occurs because the dynamics first approach a low-rank stable point with non-uniform support—that is, a point where $\hat{a}_i = 0$ for some $i \in [K-1]$ and among the non-zero entries, $\hat{a}_i \neq \hat{a}_j$ for some i, j. By moving toward a non-uniform configuration, metrics such as M measuring uniformity increase. The existence of such non-uniform stable points arises from the structure of the matrix Ψ. The quantities $(\Psi a)_i$ play the role of margins in our loss function. Each singular mode $\hat{a}_j$ contributes to enlarging $K/2$ of these margins—precisely those indices $i \in [K-1]$ for which $\Psi_{ij} \neq 0$. As $\|a\|_1$ becomes large, the energy is determined, up to exponentially small terms, by the smallest normalized margins $\arg\min_i(\Psi\hat{a})_i$. While NC maximizes this quantity in the full-rank setting, in rank-constrained regimes we do not necessarily have an equal number of singular values contributing to each margin, making non-uniform solutions preferable.

For $K = 4$, all stable points are uniform on their support, ensuring standard metrics monotonically decrease. For $K \geq 8$, when non-monotonicity occurs, the trajectory remains

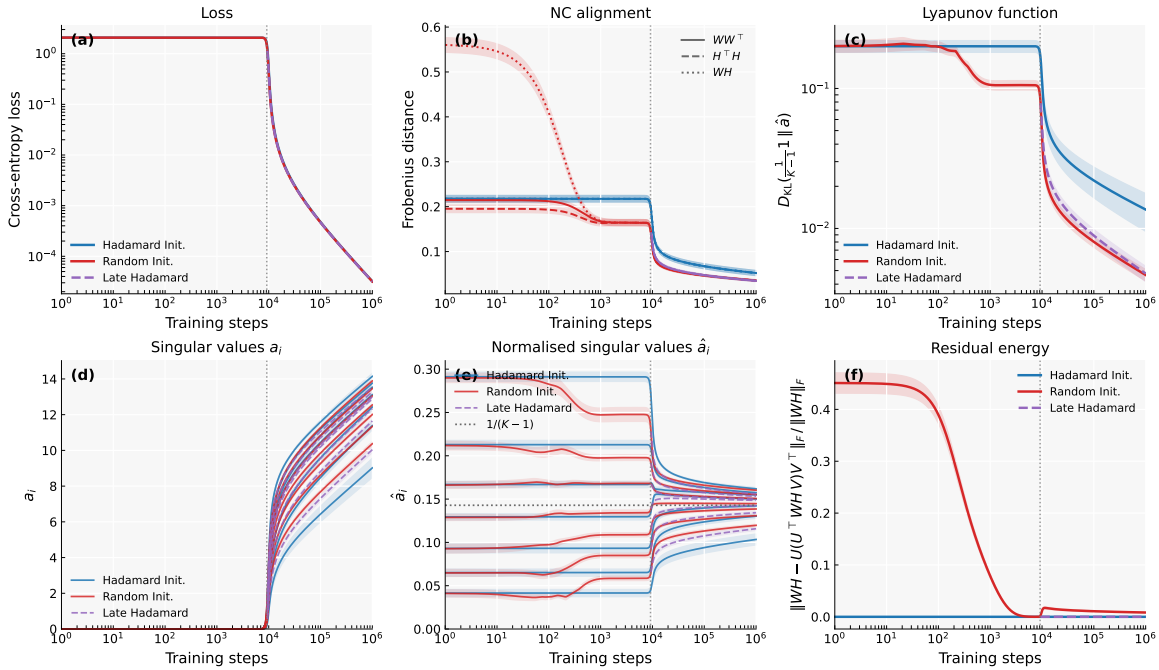

Figure 3. Gradient flow under small random initialization, Hadamard initialization with the same singular values, and late-Hadamard initialized at the end of the alignment phase (vertical dotted line). Parameters $K = 8, d = 40$. mean and std reported over ten runs.

near low-rank stable points for extended periods before transitioning to higher-rank saddles, eventually reaching NC. Similar behavior has been observed empirically (Jacot et al., 2021), albeit in settings with finite-norm critical points.

5. Numerical experiments

We now test whether these analytic trajectories capture the qualitative behavior of standard small-random initialization. Fig. 3 reports, for both random and Hadamard initialization, the metrics studied in the preceding sections, together with the residual energy defined in App. C, which measures the extent to which the singular vectors of the logit matrix are aligned with the Hadamard basis. Random trajectories exhibit a two-stage structure. First, during an initial alignment phase, the residual energy decreases while other metrics are mostly static. After this phase, both trajectories exhibit comparable qualitative trends. Fig. 3 also shows a late-Hadamard trajectory initialized after the alignment phase, using singular values matched to those of the random trajectory at that time. This late-Hadamard trajectory provides a representative trajectory of small random initialization after the alignment phase. Additional experiments are in App. C.

6. Conclusion

CE training dominates modern machine learning yet remains far less understood than MSE, even in simple settings. Under a canonical CE setup, we show that parameters grow unboundedly, exponential slowdowns near saddles persist for extended periods, natural convergence metrics behave non-monotonically, and the qualitative nature of convergence depends nontrivially on both initialization and the number of classes. None of these phenomena arise under MSE. We uncover these features by adapting the spectral-dynamics framework of Saxe et al. to the softmax setting. We view demonstrating that such an extension is feasible as our central contribution, and expect it to serve as a foundation for future CE analyses, similar to what has occurred for MSE.

Future work. Natural next steps include extending beyond $K = 2^m$, as well as extensions to regularization, alternative optimizers, and deeper networks. Most excitingly, our proof of Theorem 3.2 extends beyond softmax to any elementwise activation function, opening the door to spectral analyses in more general nonlinear architectures.

Acknowledgments

We thank the anonymous reviewers for their thoughtful feedback and constructive suggestions, which helped improve the clarity and presentation of the paper. CG is supported by the Charles Coulson Scholarship. The authors also acknowledge support from His Majesty's Government in the development of this research. CT acknowledges support by the NSERC Discovery Grant No. 2021-03677, the Alliance Grant ALLRP 581098-22 and a gift from Google. For the purpose of Open Access, the authors have applied a CC BY public copyright license to any Author Accepted Manuscript (AAM) version arising from this submission.

Impact Statement

This paper presents work whose goal is to advance the field of machine learning. There are many potential societal consequences of our work, none which we feel must be specifically highlighted here.

References

Braun, L., Dominé, C., Fitzgerald, J., and Saxe, A. Exact learning dynamics of deep linear networks with prior knowledge. In *Advances in Neural Information Processing Systems*, volume 35, pp. 6615–6629. Curran Associates, Inc., 2022. URL https://proceedings.neurips.cc/paper_files/paper/2022/file/2b3bb2c95195130977a51b3bb251c40a-Paper-Conference.pdf.

Cohen, N. and Razin, N. Lecture notes on linear neural networks: A tale of optimization and generalization in deep learning. *arXiv preprint arXiv:2408.13767*, 2024.

Domin'e, C. C. J., Anguita, N., Proca, A. M., Braun, L., Kunin, D., Mediano, P. A. M., and Saxe, A. From lazy to rich: Exact learning dynamics in deep linear networks. *ArXiv*, abs/2409.14623, 2024. URL https://api.semanticscholar.org/CorpusID:272826705.

Garrod, C. and Keating, J. P. The persistence of neural collapse despite low-rank bias: An analytic perspective through unconstrained features. *ArXiv*, abs/2410.23169, 2024a. URL https://api.semanticscholar.org/CorpusID:273695529.

Garrod, C. and Keating, J. P. Unifying low dimensional observations in deep learning through the deep linear unconstrained feature model. *arXiv preprint arXiv:2404.06106*, 2024b.

Gidel, G., Bach, F., and Lacoste-Julien, S. Implicit regularization of discrete gradient dynamics in linear neural networks. In *Advances in Neural Information Processing Systems*, volume 32. Curran Associates, Inc., 2019. URL https://proceedings.neurips.cc/paper_files/paper/2019/file/f39ae9ff3a81f499230c4126e01f421b-Paper.pdf.

Horadam, K. J. *Hadamard matrices and their applications*. Princeton university press, 2012.

Jacot, A., Ged, F., Şimşek, B., Hongler, C., and Gabriel, F. Saddle-to-saddle dynamics in deep linear networks: Small initialization training, symmetry, and sparsity. *arXiv preprint arXiv:2106.15933*, 2021.

Ji, W., Lu, Y., Zhang, Y., Deng, Z., and Su, W. J. An unconstrained layer-peeled perspective on neural collapse. In *International Conference on Learning Representations*, 2022. URL https://openreview.net/forum?id=WZ3yjh8coDg.

Ji, Z. and Telgarsky, M. Gradient descent aligns the layers of deep linear networks. In *International Conference on Learning Representations*, 2019. URL https://openreview.net/forum?id=HJflg30qKX.

Ji, Z. and Telgarsky, M. Directional convergence and alignment in deep learning. In *Advances in Neural Information Processing Systems*, volume 33, pp. 17176–17186. Curran Associates, Inc., 2020. URL https://proceedings.neurips.cc/paper_files/paper/2020/file/c76e4b2fa54f8506719a5c0dc14c2eb9-Paper.pdf.

Kunin, D., Ravent'os, A., Domin'e, C. C. J., Chen, F., Klindt, D., Saxe, A., and Ganguli, S. Get rich quick: exact solutions reveal how unbalanced initializations promote rapid feature learning. *ArXiv*, abs/2406.06158, 2024. URL https://api.semanticscholar.org/CorpusID:270371640.

Lee, J. D., Panageas, I., Piliouras, G., Simchowitz, M., Jordan, M. I., and Recht, B. First-order methods almost always avoid strict saddle points. *Mathematical programming*, 176(1):311–337, 2019.

Lyu, K. and Li, J. Gradient descent maximizes the margin of homogeneous neural networks. *arXiv preprint arXiv:1906.05890*, 2019.

Mainali, N. and Teixeira, L. Exact learning dynamics of in-context learning in linear transformers and its application to non-linear transformers. *ArXiv*, abs/2504.12916, 2025. URL https://api.semanticscholar.org/CorpusID:277857272.

Mixon, D. G., Parshall, H., and Pi, J. Neural collapse with unconstrained features. *Sampling Theory, Signal Processing, and Data Analysis*, 20, 2020. URL https://api.semanticscholar.org/CorpusID:227127383.

Papyan, V., Han, X., and Donoho, D. L. Prevalence of neural collapse during the terminal phase of deep learning training. *Proceedings of the National Academy of Sciences of the United States of America*, 117:24652 – 24663, 2020. URL https://api.semanticscholar.org/CorpusID:221172897.

Saxe, A. M., McClelland, J. L., and Ganguli, S. Exact solutions to the nonlinear dynamics of learning in deep linear neural networks. *CoRR*, abs/1312.6120, 2013. URL https://api.semanticscholar.org/CorpusID:17272965.

Saxe, A. M., McClelland, J. L., and Ganguli, S. A mathematical theory of semantic development in deep neural networks. *Proceedings of the National Academy of Sciences*, 116(23):11537–11546, 2019. doi: 10.1073/pnas.1820226116. URL https://www.pnas.org/doi/abs/10.1073/pnas.1820226116.

Soudry, D., Hoffer, E., Nacson, M. S., Gunasekar, S., and Srebro, N. The implicit bias of gradient descent on separable data. *Journal of Machine Learning Research*, 19 (70):1–57, 2018. URL http://jmlr.org/papers/v19/18-188.html.

Thrampoulidis, C., Kini, G. R., Vakilian, V., and Behnia, T. Imbalance trouble: Revisiting neural-collapse geometry. *Advances in Neural Information Processing Systems*, 35: 27225–27238, 2022.

Vardi, G., Shamir, O., and Srebro, N. On margin maximization in linear and relu networks. *Advances in Neural Information Processing Systems*, 35:37024–37036, 2022.

Zhu, Z., Ding, T., Zhou, J., Li, X., You, C., Sulam, J., and Qu, Q. A geometric analysis of neural collapse with unconstrained features. *Advances in Neural Information Processing Systems*, 34:29820–29834, 2021.

A. Summary of notations

Table 1. Summary of Key Notations

Notation	Description	Context / Definition
K	Number of classes.	Assumed to be $K = 2^m$.
n	Number of samples per class.	Assumed to be balanced.
W	Last-layer weight matrix.	$\mathbb{R}^{K\times d}$
H	Feature matrix.	$\mathbb{R}^{d\times Kn}$
Z	Logit matrix.	$Z = WH$
Y	One-hot label matrix.	$Y = I_K \otimes 1_n^T$
$P(Z)$	Softmax matrix.	Softmax applied columnwise to Z.
S	Simplex ETF matrix.	$S = I_K - \frac{1}{K}1_K 1_K^T$
Φ	Sylvester Hadamard matrix.	$\mathbb{R}^{K\times K}$ matrix (Def. 3.1).
Ψ	Reduced dynamics matrix.	$1_{K-1}1_{K-1}^T - \Phi[2:K, 2:K]$.
U, V	Left/Right singular vector matrices.	$U = V = \frac{1}{\sqrt{K}}\Phi$ for Hadamard Init.
α_i, β_i	Singular values.	Non-trivial singular values of W and H.
a	Logit singular values (vector).	$a = (a_1, \dots, a_{K-1})$, $a_i = \alpha_i\beta_i$.
$\hat{a}$	Normalized logit singular values.	$\hat{a}_i = a_i/\|a\|_1$.
b, D	Terms in reduced dynamics.	Defined in Eq. 4.
M	L_2-based metric for NC.	Measures distance from $\hat{a}$ to uniform (Eq. 7).
D_{KL}	KL divergence.	Used as a Lyapunov function (Thm. 4.1).

Throughout, $\mathbb{R}$ denotes the reals and $\mathbb{N}$ the natural numbers. For a positive integer j, we write $[j] = \{1, \dots, j\}$, and $e_\ell \in \mathbb{R}^j$ denotes the ℓ-th standard basis vector. I_k represents the $k \times k$ identity matrix, and 1_k denotes an all-ones vector of dimension k. For a given matrix A, A^T is its transpose, and $A[i_1 : i_2, j_1 : j_2]$ indicates the submatrix sliced from rows i_1 to i_2 and columns j_1 to j_2. The operator $\mathrm{diag}(v)$ forms a diagonal matrix using the elements of vector v. We use $\otimes$ for the Kronecker product, $\odot$ for the Hadamard (elementwise) product and $\oplus$ for the bitwise XOR. Finally, $\|\cdot\|_F$, and $\|\cdot\|_1$ denote the Frobenius norm and the L_1 norm, respectively. Some key notation is summarized in Table 1.

B. Proofs

B.1. Proof of Theorem 3.2

Let ϕ_i, $i \in \{1, 2, \dots, K\}$, be the rows of the $K \times K$ Sylvester–Hadamard matrix Φ. We use the following "closure" property (Lemma 3.6 of Horadam (2012)), where $i \oplus j$ denotes bitwise XOR:

Fact 1. For any $i, j \in \{1, \dots, K\}$, it holds that $\phi_i \odot \phi_j = \phi_{i\oplus j}$.

For all $i \in [K]$, define matrices $\Phi_i := \Phi\,\mathrm{diag}\,(\phi_i) = \left[\phi_j^T \odot \phi_i^T\right]_{j\in[K]}$. Note that $\Phi_1 = \Phi$. Using Fact 1, we can express each Φ_i in terms of a corresponding permutation matrix $\Pi_i = \left[e_{i\oplus j}^T\right]_{j\in[K]}$, where $e_\ell \in \mathbb{R}^K$ denotes the ℓ-th standard basis vector:

$$\Phi_i := \Phi\,\mathrm{diag}\,(\phi_i) = \Pi_i\Phi, \qquad \text{for all } i \in [K]. \tag{8}$$

Recall that softmax is applied columnwise. Thus, to prove the advertised identity it suffices for any column $i \in [K]$ that

$$P(\frac{1}{K}\Phi\,\mathrm{diag}\,(a)\,\phi_i) = \frac{1}{K}\Phi\,\mathrm{diag}\left(\Phi P(\frac{1}{K}\Phi a)\right)\phi_i\,.$$

Using the property $\mathrm{diag}\,(u)\cdot v = \mathrm{diag}\,(v)\cdot u$ for any u, v on both sides of the equality, and applying Eq. (8), this is equivalent to

$$P(\frac{1}{K}\Pi_i\Phi a) = \frac{1}{K}\Pi_i\Phi\Phi P(\frac{1}{K}\Phi a)\,.$$

Since $\Phi\Phi = \Phi\Phi^T = KI_K$, this claim reduces to $P(\frac{1}{K}\Pi_i\Phi a) = \Pi_i P(\frac{1}{K}\Phi a)$, which holds by permutation equivariance of the softmax.

B.2. Proof of Theorem 3.3

Recall $U = \frac{1}{\sqrt{K}}\Phi$, where Φ is the $K \times K$ Sylvester Hadamard matrix, and that we initialize our parameter matrices as: $W = UD_W R^T$, $H = RD_H V^T$, where $R \in \mathbb{R}^{d\times d}$ is orthogonal, and $V = U \otimes Q$ is orthogonal, with Q being a right singular matrix of 1_n^T, meaning it obeys the relation: $1_n^T = \sqrt{n} e_1^{(n)T} Q^T$, where $e_1^{(n)}$ is the first standard basis vector in $\mathbb{R}^n$. Also recall that $D_W \in \mathbb{R}^{K\times d}$ has its only non-zero singular values given by $\alpha_1, \dots \alpha_K$, and $D_H \in \mathbb{R}^{d\times Kn}$ has its only non-zero singular values given by $\beta_1, \dots, \beta_K$. Note as a consequence of the definitions of U, V, we can write $Y = \sqrt{n} U[I_K, 0_{K\times K(n-1)}]V^T$.

We also have at initialization that the logit matrix is given by

$$Z = UD_W D_H V^T.$$

Note that $D_W \in \mathbb{R}^{K\times d}$ and $D_H \in \mathbb{R}^{d\times Kn}$. Hence, defining $D_Z = D_W D_H \in \mathbb{R}^{K\times Kn}$, and $D_a = \text{diag}(a_1, ..., a_K)$, where $a_i = \alpha_i \beta_i$, this matrix can be written as:

$$D_Z = [D_a, 0_{K\times K(n-1)}] = D_a \otimes e_1^{(n)T}.$$

Hence we can write

$$Z = U\left(D_a \otimes e_1^{(n)T}\right)(U \otimes Q)^T = U\left[(D_a U^T) \otimes (e_1^{(n)T} Q^T)\right].$$

Next, using that $1_n^T = \sqrt{n} e_1^{(n)T} Q^T$, this becomes:

$$Z = \frac{1}{\sqrt{n}} U\left[(D_a U^T) \otimes 1_n^T\right].$$

Then using that this has repeated columns, this becomes:

$$Z = (UD_{\tilde{a}} U^T) \otimes 1_n^T,$$

where we define $\tilde{a} = \frac{1}{\sqrt{n}} a$. Since this is the same matrix as $UD_{\tilde{a}}U^T$, just with repeated columns, we can apply Theorem 3.2 to calculate the softmax matrix at initialization:

$$P(Z) = (UD_{\tilde{\nu}} U^T) \otimes 1_n^T,$$

where

$$\tilde{\nu}_i = \frac{\sum_j \Phi_{ij} e^{\frac{1}{K}(\Phi\tilde{a})_j}}{\sum_j e^{\frac{1}{K}(\Phi\tilde{a})_j}}.$$

Now consider the gradient flow equations of our model

$$\frac{dW}{dt} = (Y - P)H^T, \qquad \frac{dH}{dt} = W^T(Y - P).$$

Consider the change of variable given by $W = U\tilde{W}$, $H = \tilde{H}V^T$, these have evolution equations given by:

$$\frac{d}{dt}(\tilde{W}) = U^T(Y - P)V\tilde{H}^T, \qquad \frac{d}{dt}(\tilde{H}) = \tilde{W}^T U^T (Y - P)V.$$

Note that, by construction, both the matrices Y, P can be written in SVD form through the matrices U, V

$$Y = \sqrt{n} U D_Y V^T, \qquad P = \sqrt{n} U D_P V^T,$$

where $D_Y = [I_K, 0_{K\times K(n-1)}] \in \mathbb{R}^{K\times Kn}$ and $D_P = [\text{diag}(\tilde{\nu}), 0_{K\times K(n-1)}] \in \mathbb{R}^{K\times Kn}$, and so

$$U^T(Y - P)V = \sqrt{n}[\text{diag}(1_K - \tilde{\nu}), 0_{K\times K(n-1)}],$$

label this matrix as B. Now returning to the evolution equations for $\tilde{H}$ and $\tilde{W}$, we label the rows of $\tilde{W}$ by $\tilde{w}_a$, and the columns of $\tilde{H}$ by $\tilde{h}_a$. These have evolution equations given by:

$$\frac{d}{dt}((\tilde{w}_i)_j) = \sum_x B_{ix}(\tilde{h}_x)_j, \qquad \frac{d}{dt}((\tilde{h}_j)_i) = \sum_x B_{xj}(\tilde{w}_x)_i.$$

Now using that $B_{ix} = \sqrt{n}(1-\tilde{\nu}_i)\delta_{ix}$ gives:

$$\frac{d}{dt}((\tilde{w}_i)_j) = \sqrt{n}(1-\tilde{\nu}_i)(\tilde{h}_i)_j, \qquad \frac{d}{dt}((\tilde{h}_j)_i) = \sqrt{n}(1-\tilde{\nu}_j)(\tilde{w}_j)_i, \tag{9}$$

where in the second of these equations if $j > K$ the derivative is zero.

Note that using our initialization scheme, we have at initialization $\tilde{w}_i = \alpha_i r_i$, $\tilde{h}_i = \beta_i r_i$, for $i = 1, \ldots, K$, and 0 otherwise, where r_i are the columns of R. One observes from Eq. (9) that the derivatives also point in the same direction. Hence this property is maintained at all times, meaning the vectors $\tilde{w}_i, \tilde{h}_i$ only evolve in their coefficients, not in their directions. These coefficients then evolve as:

$$\frac{d}{dt}(\alpha_i) = \sqrt{n}(1-\tilde{\nu}_i)\beta_i, \qquad \frac{d}{dt}(\beta_i) = \sqrt{n}(1-\tilde{\nu}_i)\alpha_i.$$

Translating back to our original parameter matrices W, H, these are the evolution equations for their singular values, and the singular vectors are frozen for all times.

It remains to demonstrate these equations take the exact form in the theorem statement. Note from the expression of $\tilde{\nu}_i$ we have

$$1-\tilde{\nu}_i = \frac{1}{\sum_j e^{\frac{1}{K}(\Phi\tilde{a})_j}} \left[\sum_j (1-\Phi_{ij}) e^{\frac{1}{K}(\Phi\tilde{a})_j} \right].$$

Then dividing the numerator and denominator by $\exp(\frac{1}{K}\sum_j \tilde{a}_j)$, gives:

$$1-\tilde{\nu}_i = \frac{1}{\sum_j e^{-\frac{1}{K}([1_K 1_K^T - \Phi]\tilde{a})_j}} \left[\sum_j [1_K 1_K^T - \Phi]_{ij} e^{-\frac{1}{K}([1_K 1_K^T - \Phi]\tilde{a})_j} \right] = \frac{b_i}{D},$$

Once we recall that $\tilde{a}_i = \frac{1}{\sqrt{n}} a_i$, this gives

$$\frac{d\alpha_i}{dt} = \frac{\sqrt{n}}{D} b_i \beta_i, \quad \frac{d\beta_i}{dt} = \frac{\sqrt{n}}{D} b_i \alpha_i,$$

where, for $a_i = \alpha_i \beta_i$:

$$b_i = \sum\nolimits_{j\in[K]} [1_K 1_K^T - \Phi]_{ij}\, e^{-\frac{1}{K\sqrt{n}}([1_K 1_K^T - \Phi]a)_j}, \quad D = \sum\nolimits_{j\in[K]} e^{-\frac{1}{K\sqrt{n}}([1_K 1_K^T - \Phi]a)_j}.$$

The first row and column of Φ consist of all ones. Since $[1_K 1_K^T - \Phi]_{1j} = 0$ for all j, it follows that $b_1 = 0$, and therefore α_1, β_1 remain constant. Moreover, since $[1_K 1_K^T - \Phi]_{j1} = 0$ for all j, these trivial singular values do not appear in the evolution equations for the others. We may thus, without loss of generality, set $\alpha_1 = \beta_1 = 0$ and henceforth take $\alpha, \beta \in \mathbb{R}^{K-1}$ to be the vectors of non-trivial singular values, with indices shifted accordingly. Consequently, define $\Psi \in \mathbb{R}^{K-1\times K-1}$ by deleting the first column and row of $1_K 1_K^T - \Phi$, so that $\Psi = 1_{K-1} 1_{K-1}^T - X$, where $X = \Phi[2:K, 2:K]$ is the core of the Sylvester Hadamard matrix.

It is simple to verify these equations have the conserved quantities $\alpha_i^2 - \beta_i^2 = C_i$. For simplicity, and following common practice (Cohen & Razin, 2024; Saxe et al., 2013; 2019; Gidel et al., 2019), we adopt the balancedness condition that sets $C_i = 0$, thus $\alpha_i = \beta_i$ throughout. Under the balancedness condition $\alpha_i = \beta_i$, we have that the logit singular values evolve as

$$\frac{da_i}{dt} = \frac{d\alpha_i}{dt}\beta_i + \alpha_i \frac{d\beta_i}{dt} = \frac{\sqrt{n}}{D} b_i(\alpha_i^2 + \beta_i^2) = \frac{2\sqrt{n}}{D} b_i a_i.$$

Then redefining

$$a' = \frac{1}{K\sqrt{n}} a, \quad t' = 2t\sqrt{n},$$

gives the gradient flow equations given in Eq. (4), once primes are dropped, since this represents a simple rescaling that does not change phenomenology.

B.3. Proof of Theorem 4.1

The KL divergence $D_{\mathrm{KL}}(p \,\|\, q) = \sum_i p_i \log\left(\frac{p_i}{q_i}\right)$ between two categorical distributions with probabilities p and q is non-negative and equals zero if and only if $p = q$. In our setting, we have:

$$D_{\mathrm{KL}}\Big(\frac{1}{K-1}1_{K-1} \,\|\, \hat{a}\Big) = -\log(K-1) - \frac{1}{K-1}\sum_i \log(\hat{a}_i).$$

For the remainder of the proof we denote this by D_{KL}. Differentiating and using Eq. (6), we obtain

$$\frac{d}{dt}\left(D_{\mathrm{KL}}\right) = -\frac{1}{K-1}\sum_i \frac{1}{\hat{a}_i}\frac{d}{dt}(\hat{a}_i) = -\frac{1}{(K-1)D}\left[\left(\sum_i b_i\right) - (K-1)\bar{b}\right], \tag{10}$$

We now define $x_i = (\Psi a)_i$ and rewrite the derivative in terms of these variables, which recall play the role of margins. First observe that

$$\bar{b} = \sum_i \hat{a}_i b_i = \sum_{ij} \hat{a}_i \Psi_{ij} e^{-(\Psi a)_j} = \frac{1}{\|a\|_1}\sum_{ij} a_i \Psi_{ij} e^{-(\Psi a)_j} = \frac{1}{\|a\|_1}\sum_j x_j e^{-x_j}. \tag{11}$$

Second note

$$\sum_i b_i = \sum_{ij} \Psi_{ij} e^{-(\Psi a)_j} = K\sum_j e^{-(\Psi a)_j} = \left(\sum_i (\Psi\hat{a})_i\right)\sum_j e^{-(\Psi a)_j},$$

where we used $\sum_i \Psi_{ij} = K = \sum_i (\Psi\hat{a})_i$. Hence, we obtain

$$\sum_i b_i = \frac{1}{\|a\|_1}\Big(\sum_i x_i\Big)\Big(\sum_j e^{-x_j}\Big). \tag{12}$$

Substituting Eqns. (11) and (12) into Eq. (10) yields

$$\frac{d}{dt}(D_{\mathrm{KL}}) = \frac{1}{(K-1)D\|a\|_1}\left[(K-1)\sum_j x_j e^{-x_j} - \left(\sum_i x_i\right)\left(\sum_j e^{-x_j}\right)\right].$$

Now, the bracketed term can be rewritten as $\frac{1}{2}\sum_{ij}(x_i - x_j)\left(e^{-x_i} - e^{-x_j}\right)$, yielding

$$\frac{d}{dt}(D_{\mathrm{KL}}) = \frac{1}{2(K-1)D\|a\|_1}\sum_{ij}(x_i - x_j)\left(e^{-x_i} - e^{-x_j}\right).$$

For each pair (i, j), the terms $x_i - x_j$ and $e^{-x_i} - e^{-x_j}$ have opposite signs unless $x_i = x_j$. Hence, every summand is non-positive, vanishing only when $x_i = x_j$. Hence the full sum is always non-positive, and equal to zero only if x is a uniform vector. Because $D > 0$ and $\|a\|_1 > 0$, the prefactor is strictly positive. Moreover, since Ψ is invertible and has 1_{K-1} as an eigenvector, the condition $x \propto 1_{K-1}$ implies $a \propto 1_{K-1}$, and hence $\hat{a} = \frac{1}{K-1}1_{K-1}$.

Thus $D_{\mathrm{KL}} \geq 0$ with equality only at $\hat{a} = \frac{1}{K-1}1_{K-1}$, and $\frac{d}{dt}D_{\mathrm{KL}} \leq 0$ with equality only at the same point. Consequently, D_{KL} decreases monotonically to zero, guaranteeing $\hat{a} \to \frac{1}{K-1}1_{K-1}$.

B.4. Proof of Theorem 4.2

Recall our choice of metric is given by:

$$M = \frac{1}{2}\sum_{i=1}^{K-1}\Big(\hat{a}_i - \frac{1}{K-1}\Big)^2.$$

A simple calculation, using the derivatives provided in Eq. (6), gives

$$\frac{dM}{dt} = \frac{1}{D}\sum_i \hat{a}_i^2[b_i - \bar{b}]\,. \tag{13}$$

First note that $M = 0$ in the $K = 2$ case for all positive initializations, and so trivially is monotonic. We begin by proving monotonicity for $K = 4$.

Note in $K = 4$ we have

$$\Psi = \begin{bmatrix} 2 & 0 & 2 \\ 0 & 2 & 2 \\ 2 & 2 & 0 \end{bmatrix} \implies \Psi a = \begin{bmatrix} 2a_1 + 2a_3 \\ 2a_2 + 2a_3 \\ 2a_1 + 2a_2 \end{bmatrix} \implies \exp(-\Psi a) = \begin{bmatrix} e^{-2a_1-2a_3} \\ e^{-2a_2-2a_3} \\ e^{-2a_1-2a_2} \end{bmatrix}.$$

Hence

$$\frac{1}{D}b = \frac{2}{1 + e^{-2a_1-2a_3} + e^{-2a_2-2a_3} + e^{-2a_1-2a_2}} \begin{bmatrix} e^{-2a_1-2a_3} + e^{-2a_1-2a_2} \\ e^{-2a_2-2a_3} + e^{-2a_1-2a_2} \\ e^{-2a_1-2a_3} + e^{-2a_2-2a_3} \end{bmatrix}.$$

Multiplying numerator and denominator by $\exp(2\sum_i a_i)$ gives

$$\frac{1}{D}b = \frac{2}{e^{2(a_1+a_2+a_3)} + e^{2a_1} + e^{2a_2} + e^{2a_3}} \begin{bmatrix} e^{2a_2} + e^{2a_3} \\ e^{2a_1} + e^{2a_3} \\ e^{2a_1} + e^{2a_2} \end{bmatrix}.$$

Writing $x_i = \exp(2a_i)$, this is then

$$\frac{1}{D}b = \frac{2}{x_1x_2x_3 + \sum_i x_i} \begin{bmatrix} \sum_i x_i - x_1 \\ \sum_i x_i - x_2 \\ \sum_i x_i - x_3 \end{bmatrix},$$

and then $\bar{b}$ is given by:

$$\frac{1}{D}\bar{b} = \frac{2}{x_1x_2x_3 + \sum_i x_i}[\sum_i x_i - \hat{a}\cdot x].$$

Hence using the expression for the derivative of our metric, given in Eq. (13), we arrive at:

$$\frac{dM}{dt} = \frac{2}{x_1x_2x_3 + \sum_i x_i}\sum_i \hat{a}_i^2[\hat{a}\cdot x - x_i].$$

The coefficient is strictly positive, and so to argue non-increasing we can drop it. Hence we simply need to show:

$$(\hat{a}\cdot x)\left(\sum_i \hat{a}_i^2\right) - \sum_i \hat{a}_i^2 x_i \le 0,$$

or equivalently:

$$\sum_i \hat{a}_i^2 \le \frac{\sum_i \hat{a}_i^2 x_i}{\sum_i \hat{a}_i x_i}.$$

Define the quantities:

$$q_i = \frac{\hat{a}_i x_i}{\sum_i \hat{a}_i x_i},$$

noting that they form a probability distribution. Then our inequality can be viewed as comparing the expectation of $\hat{a}$ over two different probability distributions, one with probabilities $\hat{a}$ and the other with probabilities q.

It is then simple to note that, since for any $\|a\|_1 > 0$, x_i is an increasing function of $\hat{a}_i$, the second distribution places more weight on larger values of $\hat{a}$, and so must be at least as large as the other expectation. They are only equal when there are no larger values of $\hat{a}_i$, meaning $\hat{a} = \frac{1}{K-1}1_{K-1}$. Hence the inequality is satisfied, and the metric is monotonically decreasing.

It remains to show that the metric is not necessarily monotonic decreasing for $K \ge 8$. To show this for $K = 8$, it is sufficient to note that for $a = [1, 1, 1, 1.25, 0.01, 0.01, 0.01]$ the derivative of our metric takes value $\frac{dM}{dt} \approx 7.3 \times 10^{-4}$, and so the

metric is increasing for these values. Call this specific counter-example v^*, and denote its corresponding b vector and its weighted average, by b^* and $\bar{b}^*$.

For $K > 8$, define our initialization as $a = [v^*, 0_{K-8}]$, then the derivative of our metric becomes

$$\frac{dM}{dt} = \frac{1}{D}\sum_{i=1}^{7}(\hat{v}_i^*)^2[b_i - \bar{b}], \qquad \text{where } \bar{b} = \sum_{j=1}^{7} v_i^* b_i.$$

Note that only $b_1, ..., b_7$ are necessary for the computation of the sign. We now use the lemma stated and proven at the end of this section, which gives that when a is only non-zero on at most the first $\frac{K}{2} - 1$ entries, then the first $\frac{K}{2} - 1$ entries of the b vector are just equal to double the values they would be in the $\frac{K}{2}$ dimensional case. Applying this iteratively, we get that if $K = 2^m > 8$, then

$$b_i = 2^{m-3} b_i^*, \qquad \bar{b} = 2^{m-3}\bar{b}^*, \qquad \text{for } i = 1, ..., 7,$$

and so

$$\frac{dM}{dt} = \frac{2^{m-3}}{D}\sum_{i=1}^{7}(\hat{v}_i^*)^2[b_i^* - \bar{b}^*], \qquad \text{where } \bar{b} = \sum_{j=1}^{7} v_i^* b_i,$$

but this clearly has the same sign as the counter-example in $K = 8$, and so gives a positive derivative.

This provides a counter-example in any K, but it has entries that are zero, which is not permitted. However if we consider the vector

$$a = [v^*, \epsilon 1_{K-8}],$$

then by continuity, as $\epsilon \to 0$ this tends to the positive value achieved by $a = [v^*, 0_{K-8}]$. Hence for any K there exists a non-zero value of ϵ such that $\frac{dM}{dt} > 0$ for $a = [v^*, \epsilon 1_{K-8}]$. Hence counter-examples exist in all $K \geq 8$.

It only remains to prove the following Lemma.

Lemma B.1. *Let $K = 2^m$, and $a^* \in \mathbb{R}^{K-1}$, with $b(a^*) = b^* \in \mathbb{R}^{K-1}$ and $\bar{b}^* = \sum_i \hat{a}_i^* b_i^* \in \mathbb{R}^{K-1}$. Let $a' \in \mathbb{R}^{2K-1}$ be given by $a' = [a^*, 0_K]$, and consider the evolution under the dynamics detailed in Eq. (4), but for dimension $2K$, initialized at a'. Denote the corresponding vectors $b(a'), \bar{b}(a') \in \mathbb{R}^{2K-1}$ by b' and $\bar{b}'$ respectively. Then for $i = 1, ..., K-1$, we have*

$$b_i' = 2b_i^*, \qquad \bar{b}' = 2\bar{b}^*.$$

Proof of Lemma B.1:

Let Ψ_{K-1} and Ψ_{2K-1} denote the two matrices derived from the Hadamard matrix, as defined in Sec. 3, with the subscript denoting their dimension. Using the construction in terms of Sylvester Hadamard matrices, as defined in Definition 3.1, these are related in the following way:

$$\Psi_{2K-1} = \begin{bmatrix} \Psi_{K-1} & 0_{K-1} & \Psi_{K-1} \\ 0_{K-1}^T & 2 & 21_{K-1}^T \\ \Psi_{K-1} & 21_{K-1} & 21_{K-1}1_{K-1}^T - \Psi_{K-1} \end{bmatrix}.$$

Hence

$$\Psi_{2K-1}a' = \begin{bmatrix} \Psi_{K-1} & 0_{K-1} & \Psi_{K-1} \\ 0_{K-1}^T & 2 & 21_{K-1}^T \\ \Psi_{K-1} & 21_{K-1} & 21_{K-1}1_{K-1}^T - \Psi_{K-1} \end{bmatrix} \begin{bmatrix} a^* \\ 0 \\ 0_{K-1} \end{bmatrix} = \begin{bmatrix} \Psi_{K-1}a^* \\ 0 \\ \Psi_{K-1}a^* \end{bmatrix},$$

and so

$$\exp(-\Psi_{2K-1}a) = \begin{bmatrix} \exp(-\Psi_{K-1}a^*) \\ 1 \\ \exp(-\Psi_{K-1}a^*) \end{bmatrix},$$

giving

$$b' = \Psi_{2K-1}\exp(-\Psi_{2K-1}a) = \begin{bmatrix} \Psi_{K-1} & 0_{K-1} & \Psi_{K-1} \\ 0_{K-1}^T & 2 & 21_{K-1}^T \\ \Psi_{K-1} & 21_{K-1} & 21_{K-1}1_{K-1}^T - \Psi_{K-1} \end{bmatrix} \begin{bmatrix} \exp(-\Psi_{K-1}a^*) \\ 1 \\ \exp(-\Psi_{K-1}a^*) \end{bmatrix}.$$

From this it is clear that the top $K-1$ entries of b' are given by the vector $2\Psi_{K-1}\exp(-\Psi_{K-1}a) = 2b^*$. Also note

$$\bar{b}' = \sum_j \hat{a}'_j b'_j = \sum_{j=1}^{K-1} \hat{a}^*_j b'_j = 2\bar{b}^*.$$

C. Further numerical experiments

C.1. Further details on figures in main body

C.1.1. FIG. 1

For Fig. 1, we use gradient descent with learning rate 0.01 and $1e7$ training steps, recorded at 1000 logarithmically spaced checkpoints. The initial logit singular values are sampled independently from the uniform distribution on $[0, 2]$. We then compare the evolution obtained from the full matrix dynamics with under Hadamard initialization with the reduced vector dynamics in Eq. (4). The two trajectories are initialized with the same singular values. The reduced vector ODE is solved using an adaptive Runge–Kutta method with relative tolerance 10^{-8} and absolute tolerance 10^{-10}; to compare with gradient descent, we evaluate it at continuous times $t_k = \eta k$, where k is the training step and $\eta = 0.01$ is the learning rate.

C.1.2. FIG. 3

For Fig. 3, we use $K = 8$ classes, one sample per class, and 10 random realizations. We train for $1e7$ gradient-descent steps with learning rate 0.01, using 5000 logarithmically spaced checkpoints. The random initialization is $W(0) = e^{-\delta}\frac{A_1}{\sqrt{K}}$, and $H(0) = e^{-\delta}\frac{A_0}{\sqrt{K}}$, where the entries of A_1 and A_0 are sampled independently from a standard Gaussian distribution and we here use $\delta = 12$. We also set $d = 5K$. The Hadamard initialization uses the same initial logit singular values as the corresponding random initialization, but places the singular vectors exactly in the Hadamard eigenspaces. Concretely, we initialize $W = UD_W R^T$ and $H = RD_H V^T$ as described in Theorem 3.2, $U = V = \frac{1}{\sqrt{K}}\Phi$. Recall from Sec. 3 that the singular value corresponding to the all 1s column of U is not updated by the flow; thus, as in theory, we assume without loss of generality that the respective entry of D_W, D_H is set to zero. To further ensure direct comparison to random initialization, we set the remaining $K - 1$ singular values such that $D_W = D_H$ and they are identical to the largest $K - 1$ singular values of the logit matrix from its corresponding random initialization pair. This isolates the *initial* difference between the two schemes to only the singular vectors.

The residual energy plotted in Fig. 3(f) measures $\|Z - U(U^T ZV)V^T\|_F / \|Z\|_F$, for $U = V = \Phi(1 : K, 2 : K)$. We use residual threshold 0.005 to identify the end of the alignment phase. Specifically, we first wait until the residual drops below 0.005, and then define the "burn-in time" as the first logged time at which the residual rises above 0.005 again. This choice selects the point at which the random trajectory has already passed through its closest approach to the Hadamard subspace. The late-Hadamard trajectory is then initialized at this burn-in time by matching the singular values of the random trajectory and placing the singular vectors in the Hadamard eigenspaces. The vertical dotted line in Fig. 3 indicates the average burn-in time across the 10 realizations.

C.2. Metrics used in the experiments

We track the following metrics as function of iterations:

(a) *Cross-Entropy Loss:* Plots the CE loss in Eq. (1).

(b) *Alignment Metrics:* Tracks the Frobenius norm distance between the nuclear-norm-normalized model components ($WW^T, H^T H, Z = WH$) and the ground-truth Simplex ETF S. For example for the logit matrix $Z = WH$ it plots $\left\|\frac{Z}{\|Z\|_*} - \frac{S}{\|S\|_*}\right\|_F$. For Hadamard Init., where Z and S share singular spaces, this is identical to the (square root of the) metric M in Eq. (7).

(c) *KL Divergence:* Plots the Lyapunov function from Theorem 4.1, measuring the KL divergence of the normalized logit singular values $\hat{a}$ from the uniform distribution $\frac{1}{K-1}1_{K-1}$.

(d) *Singular Values:* Plots the evolution of the raw singular values $\sigma_i(Z)$ of the logit matrix $Z = WH$. For the *Hadamard Init.* and *ODE* runs, these are equivalent to the main body's logit singular values a_i.

(e) *Normalized Singular Values:* Plots the L_1-normalized singular values $\hat{\sigma}_i(Z) = \sigma_i(Z)/\sum_j \sigma_j(Z)$. For the *Hadamard Init.* and *ODE* runs, these are equivalent to the main body's $\hat{a}_i = a_i/\|a\|_1$.

(f) *Residual Energy:* Measures the fraction of the logit matrix Z that lies outside the signal subspace of the Hadamard Init.. Specifically, for $U = V = \Phi(1 : K, 2 : K)$, it measures $\|Z - U(U^T ZV)V^T\|_F / \|Z\|_F$

We track and plot these metrics in 5000 logarithmically spaced time instants. All results are averaged over 10 runs, with the shaded regions in our plots representing the standard error of the mean.

C.3. Additional random-versus-Hadamard experiments for $K = 4$ and $K = 16$

We provide additional experiments comparing small random initialization and Hadamard initialization for $K = 4$ and $K = 16$, with $d = 5K$, in Fig. 4. These experiments complement the $K = 8$ results in Fig. 3 (setup is the same as described in Sec. C.1). In all cases, both random and Hadamard initialization exhibit a similar qualitative two-stage behavior. In the first, small-logit phase, the loss changes slowly and the singular values remain small. For random initialization, this phase also corresponds to alignment of the logit matrix toward the Hadamard subspace; for Hadamard initialization, the trajectory is already in this subspace, and the normalized singular values remain constant. In the second, large-logit phase, the singular values grow, the loss decreases, and the normalized singular values begin moving toward their limiting equilibrium. This behavior is very similar to that observed in Fig. 3 of the main text.

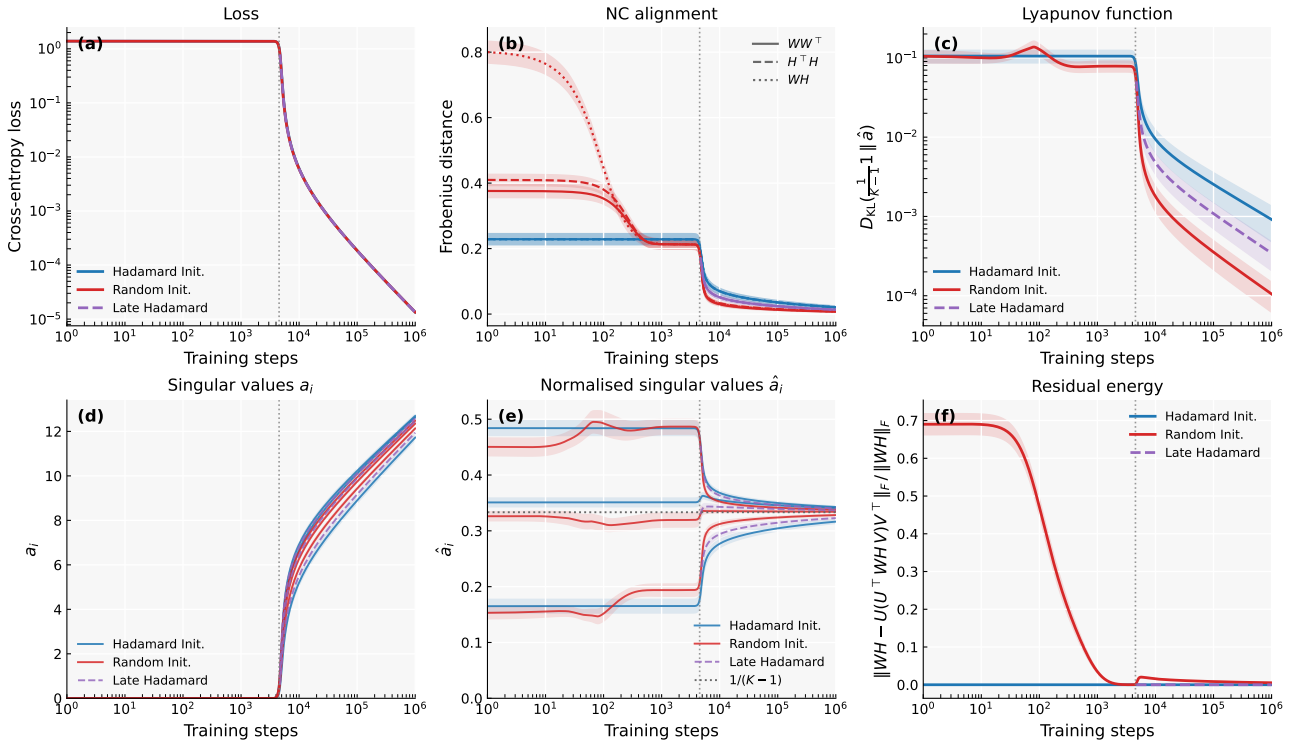

(a) $K = 4, d = 5K$

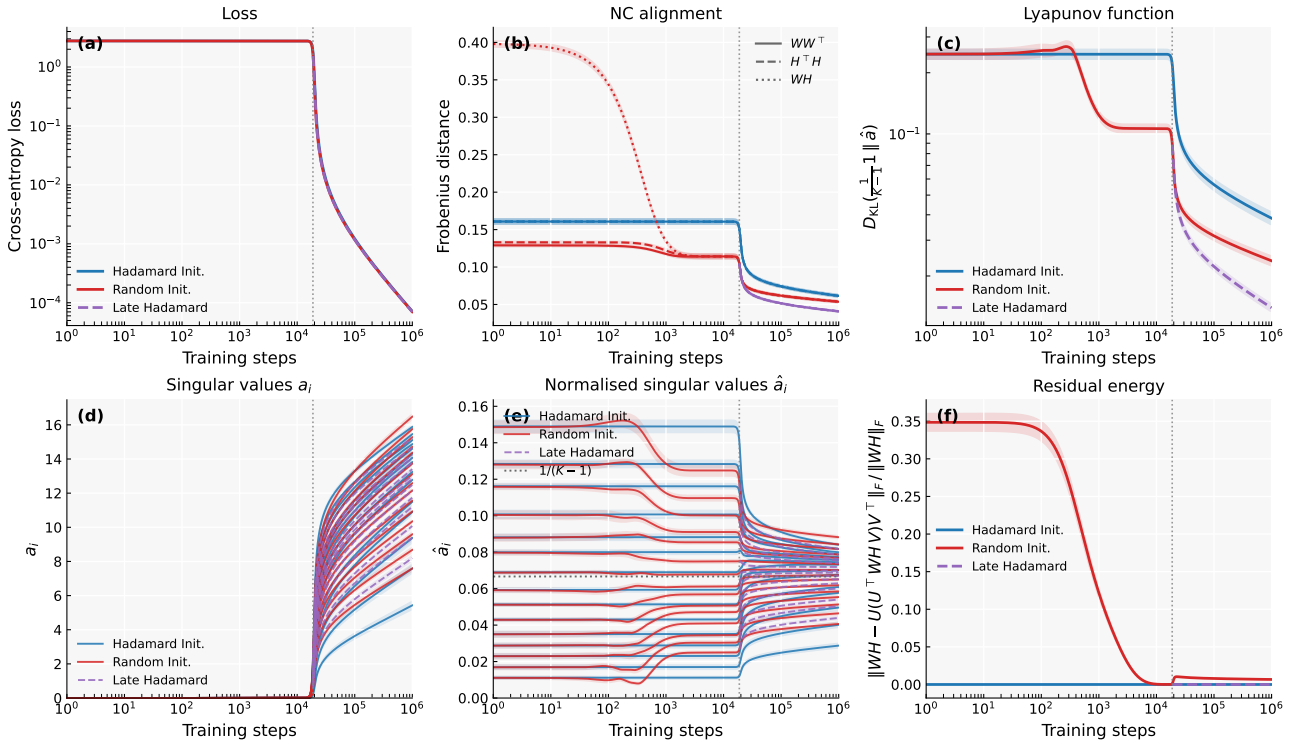

(b) $K = 16, d = 5K$

Figure 4. Additional comparison between gradient flow under small random initialization and Hadamard initialization for $K = 4$ and $K = 16$. Plots are the same as Fig. 3 other than updated class number. The two-stage behavior of random initialization is visible in both cases.